

Origin of Enhanced Electromechanical Coupling in (Yb,Al)N Nitride Alloys

Junjun Jia^{1,*} and Takahiko Yanagitani^{2,3,4,†}

¹Global Center for Science and Engineering (GCSE), Faculty of Science and Engineering, Waseda University, 3–4–1 Okubo, Shinjuku, Tokyo 169–8555, Japan

²Graduate School of Advanced Science and Engineering, Waseda University, 3–4–1 Okubo, Shinjuku, Tokyo 169–8555, Japan

³Kagami Memorial Research Institute for Materials Science and Technology, Waseda University, 2–8–26 Nishiwaseda, Tokyo 169–0051, Japan

⁴JST PRESTO, 4–1–8 Honcho, Kawaguchi, Saitama 332–0012, Japan

(Received 19 November 2020; revised 8 August 2021; accepted 7 September 2021; published 8 October 2021)

Our experiments demonstrate that alloying the cubic-phase YbN into the wurtzite-phase AlN results in clear mechanical softening and enhanced electromechanical coupling of AlN. First-principle calculations reproduce experimental results well, and predict a maximum 270% increase in electromechanical coupling coefficient caused by (1) an enhanced piezoelectric response induced by the local strain of Yb ions and (2) a structural flexibility of the (Yb,Al)N alloy. Extensive calculations suggest that the substitutional neighbor Yb-Yb pairs in wurtzite AlN are energetically stable along the *c* axis, and avoid forming on the basal plane of the wurtzite structure due to the repulsion between them, which explains why (Yb,Al)N films with high Yb concentrations are difficult to fabricate in our sputtering experiments. Moreover, the neighbor Yb-Yb pair interactions also promote structural flexibility of (Yb,Al)N, and are considered a cause for mechanical softening of (Yb,Al)N.

DOI: 10.1103/PhysRevApplied.16.044009

I. INTRODUCTION

AlN films have attracted considerable research interest for applications in electroacoustic devices, e.g., an AlN film bulk acoustic resonator (FBAR) in microwave communication, because of their high thermal stability, and high operating frequencies, high *Q* factor, and high reliability [1–3]. A major drawback is their low electromechanical coupling coefficient k_t^2 , which is considerably smaller than that of perovskite-based oxides [3,4], which leads to loss in the microwave and low-bandwidth filters. The common experimental approach to improve k_t^2 is to alloy AlN with rocksalt nitrides (ScN, YN, and Ti_{0.5}Mg_{0.5}N) [5–8]. A successful example is AlN alloying with rocksalt-structured ScN, denoted as (Sc,Al)N (Sc_xAl_{1-x}N), which shows a considerable enhancement in k_t^2 at $x = 0.43$ [9].

From the perspective of materials design, when alloying with rocksalt nitrides, a giant enhancement in k_t^2 can be considered as (1) an increase in the field-induced strain *via* the increase in the longitudinal piezoelectric constant e_{33} , and (2) the simultaneous decrease in the longitudinal elastic stiffness c_{33} based on $k_t^2 \sim e_{33}^2 / \epsilon_{33} c_{33}$, where ϵ_{33} is the dielectric constant [10]. In the (Sc,Al)N alloy, the

enhancement in k_t^2 can be attributed to the giant piezoelectric response and mechanical softening due to the structural frustration, when the rocksalt endmember ScN is added to the alloy near the phase boundary (approximately 50%) between the wurtzite and cubic phases [7,11]. In spite of the giant piezoelectric response near the phase boundary, the stability of the wurtzite phase at such high Sc concentrations is rather poor due to thermodynamic driving forces for phase separation, which leads to destruction of the piezoelectricity [12]. To improve the stability of the wurtzite phase during the fabrication, a feasible approach is to discover the alloy system with the low wurtzite-to-rocksalt transition concentration, which is expected to fabricate more easily [11]. Likewise, as an indication of mechanical softening, the elastic constant c_{33} for (Sc,Al)N decreases from 342 to 130 GPa with the Sc dopant increasing from 0% to 50% [7]. The significant softening near the phase boundary causes a reduction in the common figure of merit of the resonator [13], and thus makes the material less attractive for practical applications [14].

Alloying AlN with transition-metal nitrides as alternative materials to (Sc,Al)N has been explored [5–7]. Theoretical calculations indicate that alloying AlN with CrN [(Cr,Al)N] or YN [(Y,Al)N] produces comparable e_{33} and c_{33} with (Sc,Al)N [7], and is expected to generate a high k_t^2 . However, so far, no experimental evidence (including

*jia@aoni.waseda.jp

†yanagitani@waseda.jp

our experiments) shows that their k_t^2 values increase with increasing alloying element concentration as (Sc, Al)N does. In particular, an opposite behavior for (Cr, Al)N is observed, i.e., the k_t^2 values decrease with increasing CrN concentration, which is possibly due to phase transition from a piezoelectric to a nonpiezoelectric crystal phase [15]. Therefore, important aspects of electromechanical coupling in AlN-based piezoelectric materials require both experimental investigation and theoretical calculation.

In order to achieve the high k_t^2 value with low alloying concentration, a reasonable approach is to substitutionally dope AlN by using the impurity element with larger ionic radius and different electronic configuration. Following the abovementioned scenario, alloying AlN with YbN, designated as (Yb, Al)N ($\text{Yb}_x\text{Al}_{1-x}\text{N}$), is expected to cause a similar structural frustration to produce the mechanical softening, since YbN also has a rocksalt cubic structure ($\text{Fm}\bar{3}\text{m}$, 225), where Yb^{3+} is bonded to six equivalent N^{3-} ions and forms a mixture of corner- and edge-sharing YbN_6 octahedra. Nevertheless, Yb has a $[\text{Xe}]4f^{14}6s^2$ electronic configuration different from $[\text{Ne}]3s^23p^1$ of Al, and has a larger atomic radius than the reported transition metal nitride endmembers (ScN and CrN) [5–7]. These characteristics are considered to generate the resistance to plastic deformation and thus mitigate the excessive softening. Moreover, a larger atomic radius would be expected to produce a large internal strain, which possibly induces an increase in e_{33} .

In this study, we investigate electromechanical coupling phenomenon in (Yb, Al)N from both an experimental and theoretical perspective, and demonstrate that alloying the cubic YbN into the wurtzite AlN leads to clear mechanical softening and enhanced e_{33} , which improves k_t^2 up to approximately 10%, which is close to the reported value of 15.5% for (Sc, Al)N [9]. We also provide a fundamental understanding of such dramatic enhancement in electromechanical coupling for (Yb, Al)N.

II. EXPERIMENTAL AND COMPUTATIONAL DETAILS

The combinatorial synthesis of c -axis-oriented (Yb, Al)N films are fabricated by sputtering deposition. (Yb, Al)N films are deposited on a Ti electrode film-silica glass substrate, where a highly oriented (0001) Ti electrode film is used as the under-layer electrode to form the high-overtone bulk acoustic resonator (HBAR) structure. The film structure is characterized by x-ray diffraction (XRD) with a $2\theta - \omega$ configuration (X'Pert PRO, PANalytical). The Yb concentrations are analyzed using electron probe microanalysis (EPMA) (JXA-8230, JEOL). The k_t^2 values and the film density are determined by comparing the experimental and theoretical longitudinal wave conversion loss curves and the frequencies of the HBAR resonators [3,16].

For theoretical calculations, the structures representing hexagonal (Yb, Al)N alloys up to $x = 0.43$ are first relaxed using density-functional theory. The Vienna *ab initio* simulation package (VASP) [17] is used for structural optimization, using the generalized gradient approximation as parameterized by Perdew *et al.* for the exchange-correlation potential [18]. A $3 \times 3 \times 2$ supercell is selected, and the special quasirandom structure (SQS) [19–21] method is used to model the random distribution of Yb in the wurtzite (Yb, Al)N structure with different x values. The SQSs are generated by optimizing the locations of Yb atoms to minimize the Warren-Cowley pair short-range order parameters, which are calculated up to the sixth coordination shell. Moreover, to realistically simulate the chemical disorder of actual alloy nitrides, we constructed approximately ten SQS structures with the same Yb concentration, and selected the SQS structure with the minimum total formation energy to calculate piezoelectric and elastic tensors. The Monkhorst-Pack k -point grids are set to $3 \times 3 \times 3$. The plane wave basis set with a cutoff energy of 600 eV is adopted, and the total energies are converged to less than 10^{-9} eV for structural relaxation. The elastic and piezoelectric tensors are calculated using density-functional perturbation theory [22–25].

III. RESULTS AND DISCUSSION

A. Structural characteristics

All fabricated (Yb, Al)N films are oriented along the c axis with various rocking curve full width at half maximum (FWHM) values, as shown in Fig. 3. No phases from Yb or YbN can be found in the XRD pattern.

The calculated lattice parameters of wurtzite AlN are $a = 3.128 \text{ \AA}$ and $c = 5.015 \text{ \AA}$, which are close to reported experimental and theoretical values [26,27]. Table I shows the calculated lattice constants of (Yb, Al)N. Both the a - and c -axis lattice spacings monotonically increase with increasing Yb concentration due to the substitution of the Yb^{3+} ion (ionic radius 0.87 Å) into the host Al ion (ionic radius 0.54 Å). XRD patterns show a similar tendency, where the (0002) plane gradually shifts toward the low-angle side, demonstrating that Yb atoms are substituted into host Al sites during the nucleation and/or growth. The

TABLE I. Calculated structural parameters of (Yb, Al)N.

	a (Å)	c (Å)	c/a	ρ (g/cm ³)
AlN	3.128	5.015	1.603	3.203
$x = 0.03$	3.146 ± 0.000	5.032 ± 0.000	1.600	3.469
$x = 0.11$	3.201 ± 0.001	5.081 ± 0.002	1.596	4.211
$x = 0.17$	3.234 ± 0.005	5.156 ± 0.004	1.602	4.679
$x = 0.25$	3.295 ± 0.007	5.153 ± 0.016	1.568	5.332
$x = 0.33$	3.357 ± 0.024	5.141 ± 0.010	1.523	5.935
$x = 0.43$	3.408 ± 0.006	5.187 ± 0.014	1.523	6.490

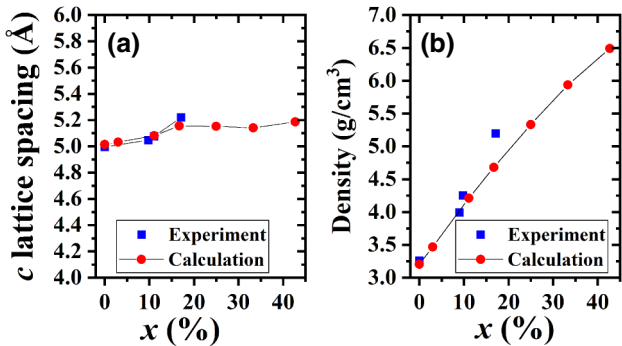


FIG. 1. The c -lattice spacing (a) and density (b) of $(\text{Yb}, \text{Al})\text{N}$ films from experimental measurement and theoretical calculation. The solid squares represent the measurement values, and the solid circles show the calculated values. Note that $(\text{Yb}, \text{Al})\text{N}$ films with high Yb concentrations ($x > 0.25$) are difficult to fabricate by sputtering.

extrapolated c -lattice constants from the precise XRD measurements are consistent with those from our first-principle calculations, as shown in Fig. 1. Moreover, our calculations show a decreasing trend in the c/a ratio, which suggests that an increase in lattice spacing along the a axis is larger than that along the c axis.

We next inquire why the c/a ratio decreases as x increases. Let us start from the question: what are the energetics involved in finding two substitutional Yb atoms in the wurtzite AlN structure? From this aspect, we calculate the pair interaction energy $\Delta E^{(n)}$ as the difference between the total energy of two n th neighbor Yb atoms and for two Yb atoms at infinite separation (twice the energy of an isolated Yb atom) [28], i.e.,

$$\Delta E^{(n)} = [E(\text{Al}_{m/2}\text{N}_{(m/2-2)}\text{Yb}_2) + E(\text{Al}_{m/2}\text{N}_{m/2})] - 2E(\text{Al}_{m/2}\text{N}_{(m/2-1)}\text{Yb}), \quad (1)$$

where n denotes the pair index and $m = 72$ is the number of atoms in the supercell. The energies correspond to the fully relaxed supercell calculations. In the calculations, an identical k mesh ($3 \times 3 \times 3$) is applied to all three total energies for consistency. The lattice parameter for all supercells has been chosen to correspond to the theoretical AlN lattice constants.

The $\Delta E^{(n)}$ are shown in Fig. 2. The result for $\Delta E^{(n=3)}$ is negative (-0.38 eV), indicating that the binding between the Yb atoms along the c axis is energetically stable. The results for $\Delta E^{(n=4)}$ and $\Delta E^{(n=6)}$ are close to zero, but remain negative. The positive $\Delta E^{(n)}$ results for $n = 1, 2$, and 5 indicate the repulsive interaction between the Yb atoms at these positions. Here, the attractive pair interaction is considered to induce the compressive stress along the c axis ($n = 3$), and the repulsive pair interaction ($n = 2$) is expected to give rise to the tensile stress along the basal plane. Thus, their superposition leads to a decreasing

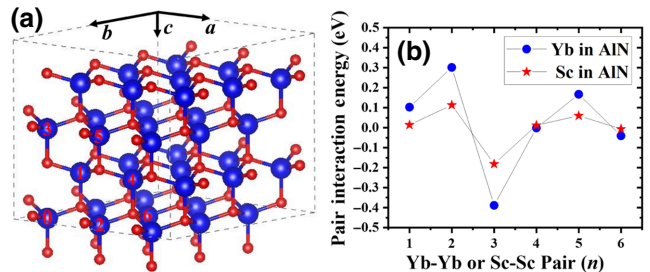


FIG. 2. (a) The six pair configurations in the $3 \times 3 \times 2$ supercell (purple, Al atoms; brown, N atoms). A Yb-Yb pair (n) is defined as the two n th neighbor substitutional Yb atoms relative to a Yb atom located at the origin “0.” (b) The pair interaction energies $\Delta E^{(n)}$ for $n = 1, 2, 3, 4, 5, 6$ neighbor Yb pairs. For comparison, $\Delta E^{(n)}$ in Sc-doped AlN is also calculated.

c/a ratio with increasing x . Note that the calculation results for $\Delta E^{(n)}$ using a bigger supercell ($5 \times 5 \times 3$) with $a = 15.64$ Å and $c = 15.04$ Å show the same tendency, suggesting that $\Delta E^{(n)}$ is an intrinsic physical parameter for the $(\text{Yb}, \text{Al})\text{N}$ alloy.

Moreover, the pair interaction energies would suggest that Yb-Yb pairing avoids $n = 1, 2, 5$ neighbor shells, and favors $n = 3, 4, 6$ neighbor configurations, especially $n = 3$. The $\Delta E^{(n)}$ in $(\text{Sc}, \text{Al})\text{N}$ show similar trends but have smaller values. For a growth process under thermal equilibrium, the Yb atoms should most likely pair into the third nearest-neighbor configurations (namely Yb-Yb pairing along the c axis) rather than be randomly distributed. This also explains our experimental observations that $(\text{Yb}, \text{Al})\text{N}$ films with high Yb concentrations ($x > 0.25$) are difficult to fabricate in sputtering experiments because the repulsion among Yb dopants in the basal plane suppresses Yb substitution into Al sites. A similar repulsion among dopants is also present in Sn-doped In_2O_3 [29–31].

Based on the above results, a SQS cell with a random distribution of Yb atoms cannot model the spatial configuration of Yb atoms in wurtzite AlN. In this study, we construct approximately ten different SQS structures with the same Yb concentration, and select the SQS structure with the minimum total formation energy to calculate its piezoelectric and elastic tensors.

B. Electromechanical coupling

Since obtaining accurate measurements for c_{33} and e_{33} along the c direction for nitride alloy films are quite difficult, especially for the thin films with a thickness of several hundred nanometers, in this study, the experimentally measured k_t^2 and acoustic wave velocity V are directly compared with the theoretically calculated values.

Because k_t^2 is known to be approximately equal to the longitudinal electromechanical coupling coefficient k_{33}^2 for the c -oriented AlN films [10], k_t^2 can be estimated by $k_t^2 \sim k_{33}^2 = e_{33}^2/\epsilon_{33}c_{33}$. In Fig. 3(a), the measured k_t^2 values

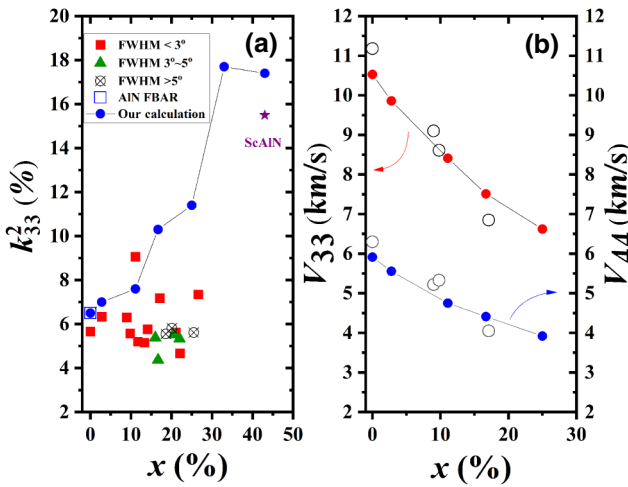


FIG. 3. (a) The calculated k_t^2 values are compared with the experimentally determined k_t^2 for (Yb, Al)N films with different rocking curve FWHM values. The smaller the FWHM value, the stronger the c -axis orientation. (b) The calculated V_{33} and V_{44} values are compared with the experimentally measured V_{33}^D and V_{44}^E for (Yb, Al)N films with FWHM $< 3^\circ$, respectively. Connected lines represent the calculated values, whereas the scattered points show the experimentally measured ones. In (a), the open square symbol represents the measurement value for the general pure AlN FBAR with Mo electrodes, and the asterisk shows the k_t^2 value for (Sc, Al)N at $x = 43\%$ [9].

are compared with the calculated k_{33}^2 values. The calculated k_{33}^2 are in good agreement with the experimentally measured tendency for k_t^2 up to $x \sim 0.11$, which increases as Yb concentration increases. The (Yb, Al)N films fabricated at various conditions show a maximal k_t^2 value of 9.05% at approximately $x = 0.11$. In contrast, our theoretical calculations suggest a maximal k_{33}^2 of 17.6% at $x = 0.33$. At high Yb concentration ($x > 0.12$), the calculated k_{33}^2 is obviously larger than the measured k_t^2 . This is most likely due to the fact that the experimentally determined k_t^2 often depends on the crystallinity of thin films and the crystal orientation, as well as the polarization direction. Moreover, as revealed by the calculations of the pair interaction energies, the repulsion between Yb-Yb pairs on the basal plane is considered to hinder further substitutional Yb doping.

Acoustic wave velocity is also a measurable experimental quantity, and it can be precisely determined by acoustic wave resonance spectra [32]. Under a constant external electric field, elastic constants (c_{33}^E and c_{44}^E) can be experimentally determined using the equations

$$c_{33}^E = \rho(V_{33}^D)^2(1 - k_{33}^2) \quad (2)$$

and

$$c_{44}^E = \rho(V_{44}^E)^2, \quad (3)$$

where ρ is the density, and V_{33}^D and V_{44}^E are longitudinal and shear acoustic wave velocities, respectively. In Fig. 3(b), the calculated V_{33} and V_{44} values are consistent with experimentally measured V_{33}^D and V_{44}^E values. Such quantitative agreement between our calculation (0 K) and the experimental results measured at room temperature allows us to expect that the acoustic phonon contribution to piezoelectricity in (Yb, Al)N alloys is small up to room temperature.

Based on the quantitative agreement between our calculation and experimentally measured results, we investigate the microscopic mechanism for the k_t^2 change with Yb concentration. The calculated dielectric constants, piezoelectric constants, and elastic moduli for (Yb, Al)N with different x are listed in Table II. With an increase in the Yb concentration, c_{33} linearly decreases up to $x = 33\%$, and a slowdown is observed from $x = 33\%$ to 43% . Our calculations reproduce the changing behavior of c_{33}^E and c_{44}^E well. Moreover, an increase in e_{33} with the alloying Yb concentration is accompanied by a decrease in c_{33} ; thus, the increasing piezoelectric response and mechanical softening are considered to cooperate to cause an increase in k_t^2 in (Yb, Al)N films.

From the microscopic perspective, e_{33} can be divided into two main contributions: (1) an electronic response to the strain of the crystal structure (clamped-ion term) and (2) the effect of internal strain on piezoelectric polarizations [27,36]. Therefore, e_{33} can be expressed as

$$e_{33}(x) = e_{33}^{\text{clamped-ion}}(x) + \frac{4eZ_{33}(x)}{\sqrt{3}a(x)^2} \frac{du}{d\sigma}, \quad (4)$$

where e is the elementary charge, a represents the equilibrium lattice parameter, Z represents the dynamical Born or transverse charge in units of e , and σ is the macroscopic applied strain. The wurtzite internal parameter is described by u , where the layered hexagonal phase differs from the wurtzite structure only in the internal parameter u between metal and nitrogen sublattices ($u = 0.5$ for the hexagonal phase, and $u \neq 0.5$ for the wurtzite phase). In Fig. 4(a), a monotonic decrease is observed for the clamped-ion term up to $x = 0.25$, followed by an increase up to -0.49 C/m^2 at $x = 0.33$. In comparison, the ionic contribution for e_{33} , which represents the local structural sensitivity to macroscopic axial strain σ , shows a clear increase with increasing Yb concentration in Fig. 4(b). Thus, an increased piezoelectric response should be mainly attributed to the internal structural strain.

To understand the ionic contribution to the piezoelectricity of (Yb, Al)N, we calculate the compositional weighted and site-resolved internal strain sensitivity and dynamic Born charge. Figure 5 shows that the internal strain sensitivity ($du/d\sigma$) around both the Al and Yb sites increases as the Yb concentration increases, and the structural strain sensitivity around Yb sites is approximately

TABLE II. Elastic (c_{ij}) and piezoelectric (e_{ij}) constants of (Yb, Al)N with different Yb concentrations x , where c_{33}^E and c_{44}^E are the experimental values for (Yb, Al)N films with FWHM < 3° in this study. Elastic constants are in gigapascals, and piezoelectric constants are in C/m². The calculated and measured c_{ij} and e_{ij} values for AlN from other groups are provided for comparison, and our calculations agree well with previous ones [27,33]. Note that ϵ_{33} is the 33 component of the dielectric tensor.

AlN	ϵ_{33}	c_{11}	c_{12}	c_{13}	c_{33}	c_{44}	c_{33}^E	c_{44}^E	e_{31}	e_{33}	k_t^2 (%)
This study											
AlN	9.76	375	128	98	355	112	384	129	-0.58	1.46	6.5
$x = 0.03$	9.97	360	128	102	337	107	-0.58	1.50	7.0
$x = 0.11$	11.16	312	124	105	298	95	298	121	-0.63	1.56	7.6
$x = 0.17$	10.99	294	129	113	264	91	226	85	-0.59	1.72	10.3
$x = 0.25$	11.67	276	123	116	234	82	-0.59	1.76	11.4
$x = 0.33$	12.84	255	139	119	192	85	-0.68	2.17	17.7
$x = 0.43$	13.15	231	126	117	182	77	-0.65	2.12	17.4
References for AlN											
Measured by Tsubouchi <i>et al.</i> [34]	...	345	125	120	395	118
Measured by McNeil <i>et al.</i> [35]	...	411 ± 10	149 ± 10	99 ± 4	389 ± 10	125 ± 5
Calculated by Xie <i>et al.</i> [33]	...	376	126	98	356	116
Calculated by Bernardini <i>et al.</i> [27]	-0.60	1.46	...

2 times larger than that around Al sites under different Yb concentrations. On the other hand, Z_{33} for Yb ions remains at approximately 3.1, and Z_{33} for Al ions remains at approximately 2.7, which vary within approximately 10% around the ionic nominal value of 3. A larger Z_{33} indicates that the Yb ion has a large polarization response to the external electric field. The abovementioned comparison suggests that the change in the ionic contribution is mainly dominated by local structural distortion caused by alloying Yb.

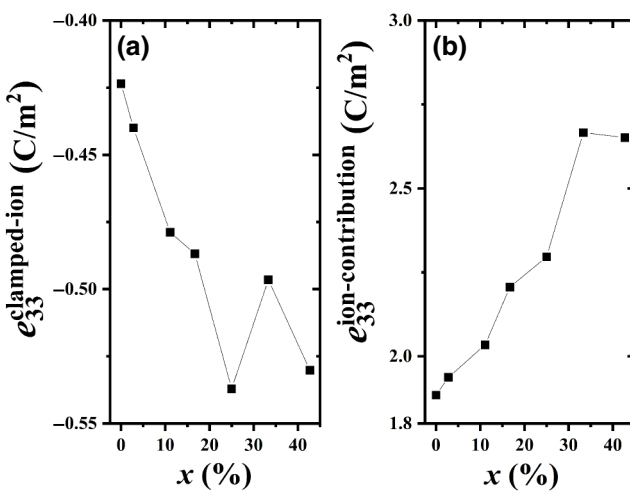


FIG. 4. Calculated contributions of e_{33} introduced in Eq. (3). (a) The clamped-ion contribution and (b) the ionic contribution, which is related to the strain effect and the Born charges Z_{33} calculated from Eq. (3).

C. Mechanical softening

From a structural point of view, AlN has a wurtzite structure (6 mm, 226), where Al^{3+} is bonded to four equivalent N^{3-} to form a corner-sharing tetrahedral structure, and YbN has a cubic structure (Fm3m, 225) with a mixture of corner- and edge-sharing octahedral structure YbN₆. The substitution of the Yb atom in Al sites is presumed to lead to structural flexibility, and then causes mechanical softening. Herein, we investigate the potential energy landscape of (Yb, Al)N at $x = 0.33$, which, in theory, has the maximal k_t^2 value.

In Fig. 6, the potential energy landscape exhibits a flat, elongated structure, which is derived by the interpolation

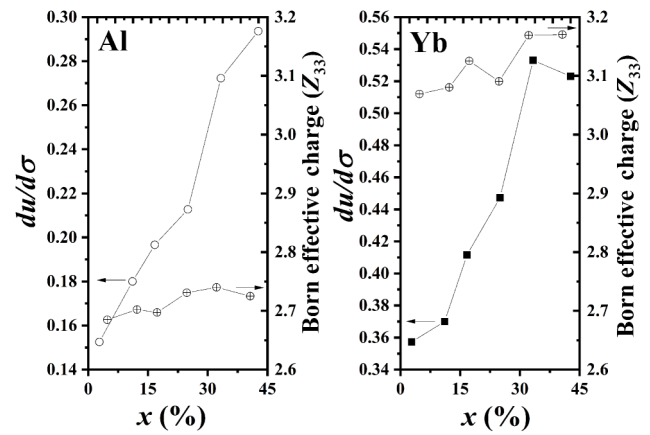


FIG. 5. Compositional weighted and site-resolved internal strain sensitivity and Born effective charges of (Yb, Al)N.

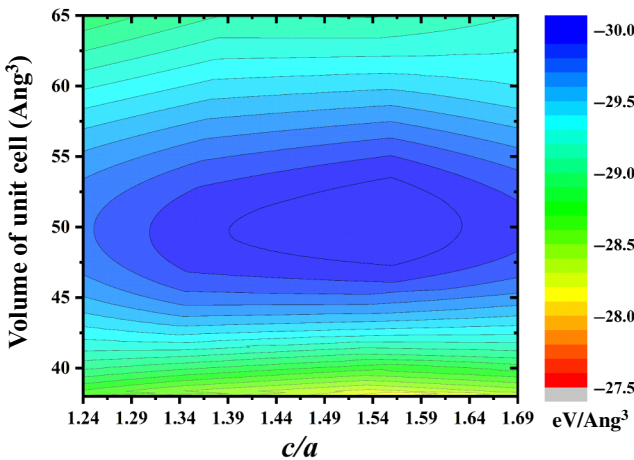


FIG. 6. Energy landscape of wurtzite (Yb, Al)N ($x = 0.33$).

of energy points in the (volume, c/a ratio) space. This landscape pattern differs from that of well-studied (Sc, Al)N [36]. In the (Sc, Al)N alloy system, the Sc atoms prefer to bind hexahedrally to nitrogen, and the resultant hexagonal ScN phase is energetically close to the wurtzite AlN phase, which acts as an energy saddle point [36,37].

To reveal the mechanical softening mechanism in the (Yb, Al)N alloy system, we investigate the local structure of the Yb atom. In the relaxed (Yb, Al)N structure ($x = 0.33$ and $c/a = 1.52$), clear local structural distortion around the Yb ion is observed, which differs from the local structure of the Al ion, as shown in Fig. 7. Depending on different local chemical environments, the Yb-N(1) bond length varies from 2.152 to 2.336 Å with an average of 2.214 Å, and the Yb-N(3) bond length varies from 2.073 to 2.279 Å with an average of 2.172 Å. Notably, Al-N tetrahedral bond lengths are 1.913 Å in the parent wurtzite AlN structure, and the longer Yb-N(1) and Yb-N(3) bond lengths in the tetrahedral Yb^{3+} structure are due to a larger ionic radius and more widely extended

electronic orbitals of Yb ions (principal quantum number $n = 6$). Moreover, the Yb-N(2) bond length varies from 2.540 to 3.249 Å with an average of 2.963 Å. The obvious difference between Yb-N(1) and Yb-N(2) ($u \neq 0.5$) suggests that (Yb, Al)N ($x = 0.33$) maintains the piezoelectric crystal phase. Furthermore, when the c/a ratio is compressed to 1.40, which is around the edge of the lowest energy contour in Fig. 6, the shortest bond lengths of Yb-N(3) on the basal plane is 2.023 Å, and the shortest bond length of Yb-N(1) is 2.142 Å. The shortest bond length of Yb-N(2) is 2.356 Å, comparable with the theoretical Yb-N bond length (2.464 Å) in the cubic YbN structure. Instead of a YbN_4 tetrahedral structure, the local structure of Yb^{3+} seems to have a deformed bipyramidal structure, which needs further investigation.

Based on the difference in bond lengths between Yb-N(1) and Yb-N(2) under external pressure ($c/a = 1.40$), a decrease in the c/a ratio with increasing x in Table I cannot be connected to the phase transition from the wurtzite ($u = 0.5$) to a quasistable layered hexagonal phase ($u \neq 0.5$), as in (Sc, Al)N [36]. Alternatively, the mechanical softening of (Yb, Al)N is attributed to structural flexibility, which is considered from the change of chemical bond type and/or orientation as well as the local structure after alloying with YbN, which flattens the energy potential landscape. Structural flexibility is beneficial to the change in wurtzite (Yb, Al)N toward a layered hexagonal phase under external pressure.

To gain more microscopic insights about the mechanical softening, the charge density difference is calculated to study the chemical interaction among constituent atoms in (Yb, Al)N with $x = 0.33$. We define the charge density difference as $\delta\rho = \rho_t - \rho_1 - \rho_2$, where ρ_t , ρ_1 , and ρ_2 are the charge densities of (Yb, Al)N, AlN, and isolated Yb atoms, respectively. In Fig. 8(a), the results of the redistribution of charge density obtained by *ab initio* calculation show that there is considerable loss of electrons between two adjacent Yb^{3+} ions, implying the existence

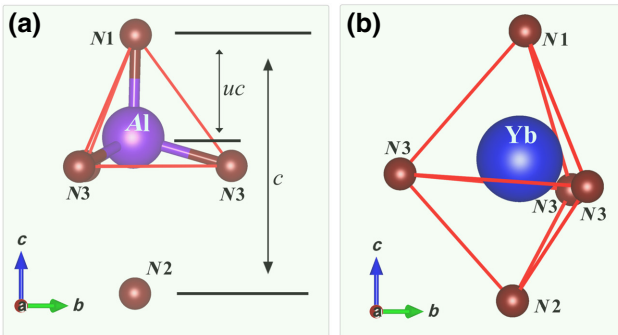


FIG. 7. Local structures of Yb and Al atoms in the relaxed (Yb, Al)N alloy system ($x = 0.33$ and $c/a = 1.52$). The index of nitrogen atoms in the local structure is given. The deformed bipyramidal structure in (b) is shown as a visual guide.

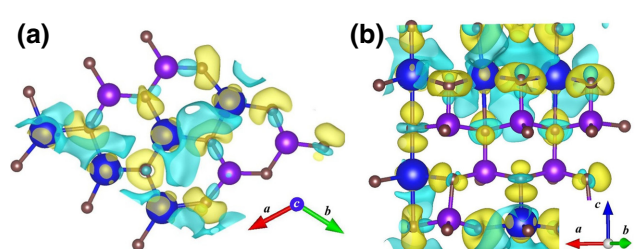


FIG. 8. Charge density differences of (Yb, Al)N with $x = 0.33$ under the compressed state of $c/a = 1.40$. (a) An a - b basal plane is selected, and (b) an a - c plane is selected to show charge density difference along the c axis. The loss of electrons is indicated in light blue and electron accumulation is indicated in yellow. Each isovalue is set to 10% of the maximum. (purple, Al atoms; blue, Yb atoms; brown, N atoms).

of repulsion between adjacent Yb^{3+} ions, which is also revealed in the calculations of the pair interaction energy ($\Delta E^{(n=2)}$), as shown in Fig. 2(b). For the wurtzite structure, any two nearby substitutional Yb ions on the a - b basal plane experience elastic repulsion due to the fact that 1) the repulsion exists between them, and 2) the Al ions around them have to relax away from the closest Yb ions (Yb^{3+} has a larger ionic size), and hence the total energy increases, i.e., repulsion. In contrast, Fig. 8(b) shows that a deformed bipyramidal structure can be formed in a certain local chemical environment, i.e., a chain configuration (-Yb-N-Yb-) along the c axis, where charges are accumulated on both sides of the N ions in the c direction with bond lengths of 2.200 and 2.464 Å for Yb-N(1) and Yb-N(2), respectively. Such a chain configuration allows N ion to attract two nearby Yb ions, and causes a decrease in the total energy, as revealed from the calculations of pair interaction energy ($\Delta E^{(n=3)}$). Owing to different bond lengths for Yb-N(1) and Yb-N(2), the deformed bipyramidal structure maintains piezoelectricity along the c axis.

In Table II, C_{11} and C_{33} rapidly decrease with increasing x , indicating structural flexibility along the a - and c -axis directions for $(\text{Yb}, \text{Al})\text{N}$ under external uniaxial stress, respectively. To understand the origin of structural flexibility at $x = 0.33$, we calculate the pair interaction energy $\Delta E^{(n)}$ under different c/a ratios. Figure 9(a) shows that $\Delta E^{(3)}$ remains negative down to $c/a = 1.35$, and then

becomes positive, indicating the elastic nature of the pair interactions. When a Yb atom is substituted into a Al site, a Yb-N(1) chemical bond is formed along the c axis, giving rise to a decrease in the total energy of the system, which has been demonstrated in our calculations (not shown here). A chain configuration of -Yb-N-Yb- can further reduce the total energy. Because the lattice spacing along the a axis is fixed in the calculations, $\Delta E^{(2)}$ and $\Delta E^{(6)}$ remain almost the same values at all c/a ratios.

On the other hand, Fig. 9(b) shows that a strong repulsive interaction exists between the Yb-Yb pair along the a axis because $\Delta E^{(2)}$ remains a large positive value for all c/a ratios with a fixed c lattice spacing. For the wurtzite structure ($u \neq 0.5$), two nearby substitutional Yb ions on the basal plane experience elastic repulsion because (1) Yb^{3+} has a larger ionic size than Al^{3+} and (2) N ions are not on the same basal plane with Yb ions. Because of the elastic nature of the attraction or repulsion shown in Fig. 9, the Yb-Yb pair interactions are considered a cause of structural flexibility in $(\text{Yb}, \text{Al})\text{N}$.

IV. CONCLUSION

Our experiments show that alloying cubic YbN into wurtzite AlN leads to enhanced electromechanical coupling in AlN, where k_t^2 is improved by 140% at $x \sim 11\%$. Theoretical calculations agree well with experimentally measured k_t^2 and elastic constants, suggesting that electromechanical coupling is mainly dominated by the local strain around Yb ions and structural flexibility caused by Yb substitution into host Al sites. Introducing more YbN into the AlN system induces mechanical softening up to $x = 43\%$. Our calculations indicate that the Yb-Yb pair interactions can contribute to such mechanical softening. The calculations of pair interaction energies also show that the Yb-Yb pairing avoids $n = 1, 2, 5$ nearest-neighbor configurations, and favors $n = 3, 4, 6$ neighbor configurations, especially $n = 3$, i.e., the Yb-Yb pair along the c axis. Alloying AlN with YbN is promising, and offers an increased k_t^2 up to approximately 10%, even at a rather low Yb concentration. Such enhancement in k_t^{22} by alloying YbN is comparable with of commercial $(\text{Sc}, \text{Al})\text{N}$.

ACKNOWLEDGMENTS

T.Y. acknowledges support from JST CREST (Grant No. JPMJCR20Q1), Japan. J.J. acknowledges funding from JSPS KAKENHI Grant-in-Aid for Scientific Research (C) (Grant No. 20K05368).

- [1] A. Muller, D. Neculoiu, G. Konstantinidis, A. Stavrinidis, D. Vasilache, A. Cismaru, M. Danila, M. Dragoman, G. Deligeorgis, and K. Tsagaraki, 6.3-GHz film bulk acoustic resonator structures based on a gallium nitride/silicon thin membrane, *IEEE Electron Device Lett.* **30**, 799 (2009).

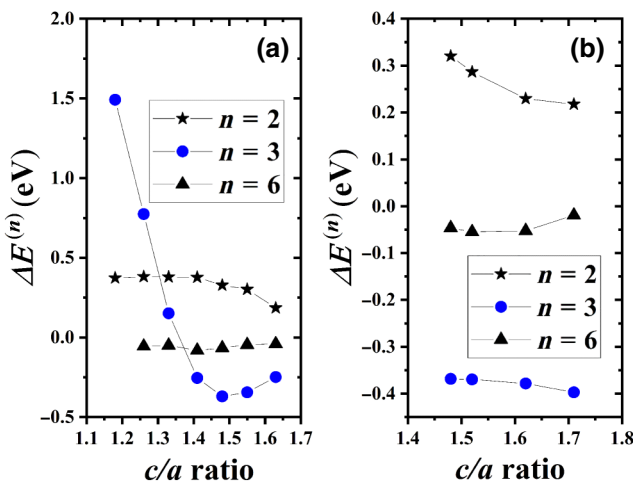


FIG. 9. Calculated pair interaction energies $\Delta E^{(n)}$ at different c/a ratios: (a) the lattice spacing along the a axis is fixed, and (b) the lattice spacing along the c axis is fixed. Here $\Delta E^{(3)}$ is the pair interaction energy due to the neighbor pair along the c axis, and $\Delta E^{(2)}$ and $\Delta E^{(6)}$ are the pair interaction energies due to the neighbor pairs on the a - b basal plane in wurtzite $(\text{Yb}, \text{Al})\text{N}$. A $3 \times 3 \times 2$ AlN structure with the lattice parameters of $(\text{Yb}, \text{Al})\text{N}$ ($x = 0.33$) is selected as the reference, and a $3 \times 3 \times 3$ k mesh is used for all the calculations.

- [2] T. Yokoyama, Y. Iwazaki, T. Nishihara, and M. Ueda, Analysis on electromechanical coupling coefficients in AlN-based bulk acoustic wave resonators based on first-principle calculations, 2012 IEEE International Ultrasonics Symposium, IEEE (2012).
- [3] T. Yanagitani and M. Suzuki, Enhanced piezoelectricity in YbGaN films near phase boundary, *Appl. Phys. Lett.* **104**, 082911 (2014).
- [4] V. M. Ristic, *Principles of Acoustic Devices* (Wiley, New York, 1983).
- [5] M. Akiyama, T. Kamohara, K. Kano, A. Teshigahara, Y. Takeuchi, and N. Kawahara, Enhancement of piezoelectric response in scandium aluminum nitride alloy thin films prepared by dual reactive cosputtering, *Adv. Mater.* **21**, 593 (2009).
- [6] M. Akiyama, K. Kano, and A. Teshigahara, Influence of growth temperature and scandium concentration on piezoelectric response of scandium aluminum nitride alloy thin films, *Appl. Phys. Lett.* **95**, 162107 (2009).
- [7] C. Tholander, I. A. Abrikosov, L. Hultman, and F. Tasnádi, Volume matching condition to establish the enhanced piezoelectricity in ternary $(\text{Sc}, \text{Y})_{0.5}(\text{Al}, \text{Ga}, \text{In})_{0.5}\text{N}$ alloys, *Phys. Rev. B* **87**, 094107 (2013).
- [8] C. Tholander, F. Tasnádi, I. A. Abrikosov, L. Hultman, J. Birch, and B. Alling, Large piezoelectric response of quaternary wurtzite nitride alloys and its physical origin from first principles, *Phys. Rev. B* **92**, 174119 (2015).
- [9] K. Umeda, H. Kawai, A. Honda, M. Akiyama, T. Kato, and T. Fukura, Piezoelectric properties of ScAlN thin films for piezo-MEMS devices, the 26th International Conference on Micro Electro Mechanical Systems (MEMS) (IEEE, Taipei, 2013), p. 582.
- [10] M. Feneberg and K. Thonke, Polarization fields of III-nitrides grown in different crystal orientations, *J. Phys. D: Appl. Phys.* **19**, 403201 (2007).
- [11] S. Manna, K. R. Talley, P. Gorai, J. Mangum, A. Zukutayev, G. L. Brennecka, V. Stevanović, and C. V. Ciobanu, Enhanced Piezoelectric Response of AlN via CrN Alloying, *Phys. Rev. Appl.* **9**, 034026 (2018).
- [12] C. Höglund, J. Birch, B. Alling, J. Bareño, Z. Czigány, P. O. Persson, G. Wingqvist, A. Žukauskaitė, and L. Hultman, Wurtzite structure $\text{Sc}_1 - x\text{Al}_x\text{N}$ solid solution films grown by reactive magnetron sputter epitaxy: Structural characterization and first-principles calculations, *J. Appl. Phys.* **107**, 123515 (2010).
- [13] R. R. Syms, H. Zou, and P. Boyle, Mechanical stability of a latching MEMS variable optical attenuator, *J. Microelectromech. Syst.* **14**, 529 (2005).
- [14] S. Manna, G. L. Brennecka, V. Stevanović, and C. V. Ciobanu, Tuning the piezoelectric and mechanical properties of the AlN system via alloying with YN and BN, *J. Appl. Phys.* **122**, 105101 (2017).
- [15] M. Suzuki and S. Kakio, Electromechanical coupling coefficient k_t^2 of Cr doped AlN films grown by sputtering deposition, 2019 IEEE International Ultrasonics Symposium (IUS), 2019, p. 716.
- [16] N. Iwata, S. Kinoshita, J. Jia, M. Suzuki, and T. Yanagitani, Experimental and theoretical investigation of k_t^2 and mechanical quality factor Q_m in YbAlN films using DFT, 2020 IEEE International Ultrasonic Symposium (IUS), 2020, p. 1.
- [17] G. Kresse and J. Furthmüller, Efficiency of *ab initio* total energy calculations for metals and semiconductors using a plane-wave basis set, *Comput. Mater. Sci.* **6**, 15 (1996).
- [18] J. P. Perdew, K. Burke, and M. Ernzerhof, Generalized Gradient Approximation Made Simple, *Phys. Rev. Lett.* **77**, 3865 (1996).
- [19] A. Zunger, S.-H. Wei, L. G. Ferreira, and J. E. Bernard, Special Quasirandom Structures, *Phys. Rev. Lett.* **65**, 353 (1990).
- [20] L. Chen, D. Holec, Y. Du, and P. H. Mayrhofer, Influence of Zr on structure, mechanical and thermal properties of Ti-Al-N, *Thin Solid Films* **519**, 5503 (2011).
- [21] A. van de Walle, P. Tiwary, M. de Jong, D. L. Olmsted, M. Asta, A. Dick, D. Shin, Y. Wang, L.-Q. Chen, and Z.-K. Liu, Efficient stochastic generation of special quasirandom structures CALPHAD: Computer coupling of phase diagrams and thermochemistry, *Calphad* **42**, 13 (2013).
- [22] D. Vanderbilt, Berry-phase theory of proper piezoelectric response, *J. Phys. Chem. Solids* **61**, 147 (2000).
- [23] X. Gonze and C. Lee, Dynamical matrices, born effective charges, dielectric permittivity tensors, and interatomic force constants from density-functional perturbation theory, *Phys. Rev. B* **55**, 10355 (1997).
- [24] X. Wu, D. Vanderbilt, and D. R. Hamann, Systematic treatment of displacements, strains, and electric fields in density-functional perturbation theory, *Phys. Rev. B* **72**, 035105 (2005).
- [25] R. D. King-Smith and D. Vanderbilt, Theory of polarization of crystalline solids, *Phys. Rev. B* **47**, 1651 (1993).
- [26] N. S. van Damme, S. M. Richard, and S. R. Winzer, Liquid-phase sintering of aluminum nitride by europium oxide additives, *J. Am. Ceram. Soc.* **72**, 1409 (1989).
- [27] F. Bernardini, V. Fiorentini, and D. Vanderbilt, Spontaneous polarization and piezoelectric constants of III-V nitrides, *Phys. Rev. B* **56**, R10024 (1997).
- [28] T. Mattila and A. Zunger, P-P and as-as isovalent impurity pairs in GaN: Interaction of deep t_2 levels, *Phys. Rev. B* **59**, 9943 (1999).
- [29] N. Yamada, I. Yasui, Y. Shigesato, H. Li, Y. Ujihira, and K. Nomura, Doping mechanism of Sn in In_2O_3 powder studied using ^{119}Sn Mössbauer spectroscopy and X-ray diffraction, *Jpn. J. Appl. Phys.* **38**, 2856 (1999).
- [30] J. Jia, A. Takaya, T. Yonezawa, K. Yamasaki, H. Nakazawa, and Y. Shigesato, Carrier densities of Sn-doped In_2O_3 nanoparticles and their effect on X-ray photoelectron emission, *J. Appl. Phys.* **125**, 245303 (2019).
- [31] J. Jia, S. Iwasaki, S. Yamamoto, S. Nakamura, E. Magome, T. Okajima, and Y. Shigesato, Temporal evolution of microscopic structure and functionality during crystallization of amorphous indium-based oxide films, *ACS Appl. Mater. Interfaces* **13**, 31825 (2021).
- [32] Y. Ohashi, M. Arakawa, J. Kushibiki, B. M. Epelbaum, and A. Winnacker, Ultrasonic microspectroscopy characterization of AlN single crystals, *Appl. Phys. Express* **1**, 077004 (2008).
- [33] M. -Y. Xie, F. Tasnádi, I. A. Abrikosov, L. Hultman, and V. Darakchieva, Elastic constants, composition, and piezoelectric polarization in $\text{In}_x\text{Al}_1 - x\text{N}$: From ab initio calculations to experimental implications for the applicability of vegard's rule, *Phys. Rev. B* **86**, 155310 (2012).

- [34] K. Tsubouchi, K. Sugai, and N. Mikoshiba, AlN material constants evaluation and SAW properties on AlN/Al₂O₃ and AlN/Si, IEEE Ultrasonic Symposium, p. 375, (1981).
- [35] L. E. McNeil, M. Grimsditch, and R. H. French, Vibrational spectroscopy of aluminum nitride, *J. Am. Ceram. Soc.* **76**, 1132 (1993).
- [36] F. Tasnádi, B. Alling, C. Hoglund, G. Wingqvist, J. Birch, L. Hultman, and I. A. Abrikosov, Origin of the Anomalous Piezoelectric Response in Wurtzite Sc_xAl_{1-x}N Alloys, *Phys. Rev. Lett.* **104**, 137601 (2010).
- [37] N. Farrer and L. Bellaiche, Properties of hexagonal ScN versus wurtzite GaN and InN, *Phys. Rev. B* **66**, 201203(R) (2002).